



Zn₃[Fe(CN)₆]₂ derived Fe/Fe₅C₂@N-doped carbon as a highly effective oxygen reduction reaction catalyst for zinc-air battery

Li Song, Tao Wang, Linghui Li, Chao Wu, Jianping He*

College of Materials Science and Technology, Jiangsu Key Laboratory of Materials and Technology for Energy Conversion, Nanjing University of Aeronautics and Astronautics, 210016, Nanjing, PR China

ARTICLE INFO

Keywords:

Iron-based catalyst
Prussian blue analogue
Carbon encapsulated metal/metal carbide
Oxygen reduction reaction
Zinc-air battery

ABSTRACT

We fabricated a highly effective oxygen reduction reaction (ORR) catalyst consisting of Fe/Fe₅C₂ species wrapped in N-doped carbon (Fe/Fe₅C₂@N-C), derived from annealing decomposition of a zwitterous Prussian blue analogue Zn₃[Fe(CN)₆]₂, which can be prepared through a facile precipitation reaction. The rationally designed carbon layer-encapsulated structure with iron/iron carbide encased inside the N-doped graphitic carbon shells is favorable for ORR, wherein the iron species not only facilitate the graphitization process but also improve the ORR activity together with outside N-doped graphitic carbon. The resultant catalyst demonstrates a positive half-wave potential ($E_{1/2}$) of 0.85 V (vs. RHE) and a nearly four-electron pathway in 0.1 M KOH solution, comparable to that of the commercial Pt/C. With superior stability to that of Pt/C, Fe/Fe₅C₂@N-C suffers almost no performance attenuation after 5000 potential cycles. The zinc-air battery using Fe/Fe₅C₂@N-C catalyst exhibits high power density and capacity, holding great promise for the practical application of metal-air batteries.

1. Introduction

Large numbers of researches have been carried out to develop alternative energy storage and conversion devices such as fuel cells and metal-air batteries. For the mass production of these promising devices, highly active cathode catalyst to enhance the efficiency of oxygen reduction reaction (ORR) is distinctly important because the sluggish kinetics at the cathode is the major technical challenge. Pt-based materials have been still by far the most efficient electrocatalyst while the scarcity, high cost and poor stability greatly limit their widespread applications. Recently intensive research efforts in reducing or replacing Pt-based catalysts have led to the development of new ORR electrocatalysts, including Pt-based alloys [1–3], metal-free carbon materials [4,5], conducting polymers [6], and transition metal/heteroatom doped carbon composites [7]. Among them, transition metal (e.g., nickel, cobalt, iron) and nitrogen doped carbon (Me-N-C) has attracted tremendous research interest as a promising electrocatalyst toward ORR [8–11]. However, in terms of the activity and durability, significant gaps between the Me-N-C and precious metal catalysts remain to be eliminated for viable application. The active sites of Me-N-C catalysts are generally speculated to be associated with N coordinated metal structures (M-N_x) with average coordination number x from 2 to 4 through X-ray absorption or Mössbauer spectroscopy techniques [12,13]. A key method for the Me-N-C catalysts to enhance the

electrocatalytic activity is to offer the sufficient exposure of the active Me-N_x sites in carbon composite materials by accurate control of the catalyst composition and structure. Despite tremendous efforts, the relatively slow kinetics of the ORR continues to be a bottleneck because of the complicated multielectron transfer process. Furthermore, some catalysts always suffer from structural degradation or catalytic centers poisoning during electrochemical processes, thus resulting in poor durability. For the Me-N-C catalysts, the metal sites are easy to fall off from the carbon matrix [14]. It is beneficial to design a highly active and durable catalyst with rich metal sites and rational core-shell structure, in which the metal sites are encased by the thin graphitic layer, not only protecting the metal sites from aggregation and dissolution, but also coupling metal sites and N-doped carbon acting as the active sites. Many researches have reported that carbon encapsulated metal or metal carbide is in favor of electrocatalysis [15–18], due to the synergistic effect between metal/metal carbide and protective nitrogen-doped graphitic layers, thus facilitating interfacial charge transfer and improving proton reduction ability [19,20].

Recently, metal-organic frameworks (MOFs) are attracting lots of interests in catalytic fields due to the unique features such as large specific surface area, controllable pore texture and tuneable composition. For example, Zhang et.al synthesized novel Co@N-C bifunctional catalysts derived from a pair of enantiotopic chiral 3D MOFs for highly efficient zinc-air battery and water splitting [17]. Prussian blue

* Corresponding author.

E-mail address: jianph@nuaa.edu.cn (J. He).

<https://doi.org/10.1016/j.apcatb.2018.11.005>

Received 16 August 2018; Received in revised form 26 October 2018; Accepted 2 November 2018

Available online 03 November 2018

0926-3373/ © 2018 Elsevier B.V. All rights reserved.

analogue, as a cyano ligand-bridged MOF, has been widely used as the precursor material in the fields of water splitting and energy storage [21–23]. Here we developed a facile strategy to synthesize highly active Fe/Fe₅C₂@N-C ORR electrocatalyst from a Prussian blue analogue Zn₃[Fe(CN)₆]₂ and applied it to the zinc-air battery. The iron species facilitate the graphitization process and improve the ORR activity together with outside N-doped graphitic carbon. In addition, the volatile zinc help to produce a porous structure and improve the dispersity of iron species during the pyrolysis process. As a result, Fe/Fe₅C₂@N-C-1000 (annealed in 1000 °C) was tested to have the highest ORR activity, comparable to that of Pt/C.

2. Experimental details

2.1. Catalysts synthesis

The Prussian blue analogue Zn₃[Fe(CN)₆]₂ was synthesized with a precipitation method. First, 6 mmol ZnCl₂ (0.818 g) was dissolved in 50 mL deionized water. Then 4 mmol K₃[Fe(CN)₆] (1.317 g) together with 0.6 g PVP (Polyvinyl Pyrrolidone, K30) was dissolved in 50 mL deionized water. The above two solutions were mixed together with 30 min magnetic stirring and kept in the dark for 6 h. The resultant brown precipitates were collected by centrifugation, consecutively washed with distilled water and ethanol and then dried at 60 °C in vacuum. Afterwards, the powders were annealed for 2 h at the temperatures of 700, 800, 900, 1000 and 1100 °C, respectively, with a ramp rate of 4 °C min⁻¹ under N₂. After carbonization, the powders were leached with 2 M HCl acid for 48 h and dried in vacuum overnight. At last, the acid-leached powders were annealed for another 2 h at the same temperatures. The above samples are noted as Fe/Fe₅C₂@N-C-X, where X refers to the pyrolysis temperature. For comparison, we prepared a control sample of Fe₃[Fe(CN)₆]₂, whose procedures were similar to Zn₃[Fe(CN)₆]₂, by replacing ZnCl₂ with FeCl₂. Fe₃[Fe(CN)₆]₂ was also used to prepare the carbonized product, noted as Fe₃[Fe(CN)₆]₂-1000, with the identical annealing and acid washing procedures like Fe/Fe₅C₂@N-C-1000.

2.2. Physical characterization

The crystallization characteristics were identified by powder X-ray diffraction (XRD) patterns measured on a Bruker D8 Advance diffractometer using a Cu Kα radiation (λ = 0.15406 nm). Scanning electron microscopy (SEM) was performed with a Hitachi S-4800 field-emission scanning electron microscope (FE-SEM) to observe the morphology. Transmission electron microscopy (TEM) and scanning transmission electron microscopy (STEM) were performed with a FEI Tecnai G2 F20 operated at 200 kV. The Brunauer-Emmett-Teller (BET) specific surface area was measured at 77 K with a Micromeritics ASAP 2050 system. X-ray photoelectron spectroscopy (XPS) analysis was carried out on a Kratos Axis Ultra DLD electron spectrometer to study the chemical composition and valence state. All the binding energies were standardized by C1 s peak energy at 284.6 eV.

2.3. Electrochemical measurements

Cyclic voltammetry (CV), rotating disk electrode (RDE) and rotating ring-disk electrode (RRDE) measurements were all conducted on a CHI760E electrochemical workstation (CH Instruments, Inc., Shanghai, China) together with a rotation speed motor (Pine Research Instrument). A standard three-electrode system was used to conduct the electrochemical tests, consisting of a catalyst ink modified RDE/RRDE, a saturated calomel electrode (SCE) and a graphite electrode, as the working electrode, reference electrode and counter electrode, respectively. The catalyst powders were first dispersed into 1 mL isopropanol containing 30 μL Nafion solution (5 wt%). Then the catalyst ink was pipetted and spread onto a polished RDE/RRDE surface to obtain the

working electrode, fixed with a total loading of 1.2 mg cm⁻². All potentials mentioned were scaled to a reversible hydrogen electrode (RHE) according to the Nernst equation. To deduct the effect of capacitive current on ORR performance, the background current of the working electrode could be obtained by running the identical measurement in Ar-saturated electrolyte and subtracted from the polarization curve in O₂ condition. Commercial Pt/C (20 wt %) was tested by the same electrochemical measurement, with the loading of 25 μg Pt cm⁻². Accelerated stressing tests (ASTs) for stability were carried out by performing CV cycling measurements between 1.0 and 0.6 V at a scan rate of 50 mV s⁻¹ at O₂-saturated condition. For RRDE tests, the hydrogen peroxide yield [H₂O₂(%)] and the electron transfer number (n) were determined from the following equations:

$$\text{H}_2\text{O}_2(\%) = 200 \frac{\frac{I_r}{N}}{I_d + \frac{I_r}{N}}$$

$$n = 4 \frac{I_d}{I_d + \frac{I_r}{N}}$$

in which I_d, I_r and N are the disk current, ring current and the current collection efficiency of the Pt ring, which was determined to be 0.40 from the reduction of K₃[Fe(CN)₆].

2.4. Zinc-air battery fabrication and testing

Ni foam was used as the current collector, which was washed with 1 M HCl solution and rinsed with distilled water and absolute ethanol to remove any oxides on the surface in advance. The zinc-air batteries were assembled in the form of 2032-type coin cell, with a polished zinc plate as the anode, an air-electrode as the cathode, 6 M KOH solution as the electrolyte and a glass-fiber film as the separator, respectively. The water-proof gas-diffusion layer was first prepared by mixing acetylene black and 60% PTFE (polytetrafluoroethylene solution with 60 wt.% solid) to a mass ratio of 1:2, the product of which was rolled to 0.4 mm thickness. To fabricate the air cathode, the catalyst powder ink was dropped on the electrolyte-facing side of the Ni foam (effective area, 0.5 cm²; catalyst loading, 1.0 mg cm⁻²), leaving the gas diffusion layer on the air-facing side. As a benchmarking battery, a Pt/C ink was also used to make up the battery with the same catalyst loading. The electrochemical data were collected with a CHI 760E electrochemical workstation and LANHE CT2001A battery test system (Wuhan LAND Electronics Ltd.) at room temperature.

3. Results and discussion

The fabrication of Fe/Fe₅C₂@N-C is on the base of wet precipitation method and subsequent heat-treatment as illustrated in Fig. 1. The Zn₃[Fe(CN)₆]₂ precipitate comes into being after the mixture of aqueous ZnCl₂ and K₃[Fe(CN)₆], forming spherical particles at the assistance of PVP. Zn₃[Fe(CN)₆]₂ is constructed by the cross-linking of zinc and the nitrogen atom within the hexacyanoferrate [Fe(CN)₆]³⁺ group, thus forming a 3D continuous framework with abundant Fe, N, C and Zn. Fig. S1 shows the Fourier transform infrared (FTIR) spectroscopy of the Zn₃[Fe(CN)₆]₂ and K₃[Fe(CN)₆]. The sharp band stretching at 2000–2200 cm⁻¹ can be identified to cyano-bridged complexes ν(CN) [24]. We can find an obvious shift of the cyanide stretching vibration mode to higher wavenumber for Zn₃[Fe(CN)₆]₂ compared with K₃[Fe(CN)₆], due to the change of coordination environment. The peaks at 1612 and 3448 cm⁻¹ should be ascribed to the O–H group bending vibration and stretching vibration of the crystal water in Zn₃[Fe(CN)₆]₂·xH₂O [25]. The two weak vibration bands at 600 and 495 cm⁻¹ are assigned to band stretching and bending of Fe–C [26]. After subjected to annealing process under N₂ atmosphere, the Zn₃[Fe(CN)₆]₂ was transformed to porous N-doped carbon with rich iron/iron carbide cores (Fe/Fe₅C₂@N-C) inside. The iron/iron carbide cores are encapsulated inside a thin graphitic carbon shell. During the pyrolysis process, zinc metal is

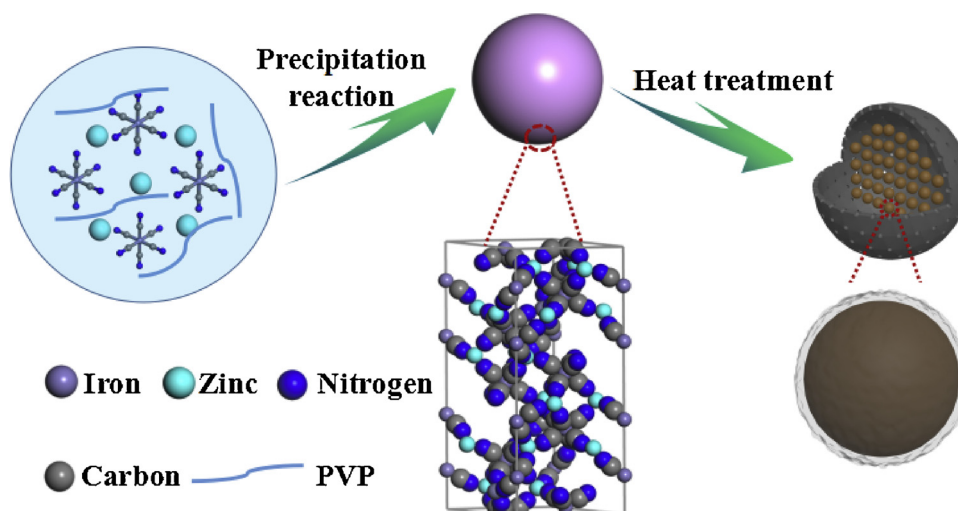


Fig. 1. The schematic demonstration of the synthesis of $\text{Zn}_3[\text{Fe}(\text{CN})_6]_2$ precursor and $\text{Fe}/\text{Fe}_5\text{C}_2@\text{N-C}$.

helpful to form porous structure and to promote the uniform distribution of iron species, which is due to the dilution effect of volatile zinc with a low boiling point of 907 °C.

The XRD patterns in Fig. 2a demonstrates that the iron species exist in the form of metallic Fe or iron carbide (Fe_5C_2) instead of iron oxide in all the $\text{Fe}/\text{Fe}_5\text{C}_2@\text{N-C}$ samples with different annealing temperatures, which are thought to be in favor of ORR [16,18]. The XRD pattern of $\text{Zn}_3[\text{Fe}(\text{CN})_6]_2$ precursor is exhibited in Fig. S2, which is corresponding to the standard pattern of $\text{Zn}_3[\text{Fe}(\text{CN})_6]_2 \cdot x\text{H}_2\text{O}$ with a face centered cubic phase (JCPDS#38-0687).

Raman spectrum of $\text{Fe}/\text{Fe}_5\text{C}_2@\text{N-C-1000}$ with a low I_D/I_G value of 1.02 indicates the crystalline nature of graphitic carbon (Fig. 2b), which is also confirmed by the XRD patterns (Fig. 2a) with a peak at 26.2° corresponding to the (002) diffraction of graphitic carbon. The graphitic carbon comes from the effect of catalytic graphitization on amorphous carbon by the Fe species [27]. The elemental composition and the valence state of $\text{Fe}/\text{Fe}_5\text{C}_2@\text{N-C-1000}$ were analyzed by X-ray photoelectron spectroscopy (XPS). In the survey spectrum as shown in Fig. 2c, four peaks centered at ~284.6, 400.6, 530.6 and 710.9 eV are assigned to C 1s, N 1s, O 1s and Fe 2p, respectively. The survey spectra for the samples with other annealing temperatures are given in Fig. S3. After carbonization, zinc content would be drastically reduced because most of the zinc would be removed either by HCl washing or volatilization due to the low boiling point, thus causing many micro-pores in the carbon matrix. The high-resolution Fe 2p spectra of $\text{Fe}/\text{Fe}_5\text{C}_2@\text{N-C-1000}$ and $\text{Zn}_3[\text{Fe}(\text{CN})_6]_2$ are analyzed to reveal the valence state of Fe. The peaks at 708.1 and 721.5 eV for the $\text{Zn}_3[\text{Fe}(\text{CN})_6]_2$ are assigned to $\text{Fe } 2p_{3/2}$ and $\text{Fe } 2p_{1/2}$ binding energy of Fe^{3+} , respectively. In the upper part of Fig. 2d, the major Fe $2p_{3/2}$ and Fe $2p_{1/2}$ peaks in pyrolytic product significantly change and split compared with its precursor, indicating a likely transformation of Fe-CN complex within $\text{Zn}_3[\text{Fe}(\text{CN})_6]_2$ to active Fe-N_x sites and iron particles embedded into carbon. Two parts of main peaks, including $2p_{3/2}$ and $2p_{1/2}$ orbitals, are found, together with a satellite peak. After deconvolution, a couple of weak peaks at around 707.3 and 720.7 eV are attributed to the binding energies of zero-valence iron (metallic iron or iron carbide) for $2p_{3/2}$ and $2p_{1/2}$ orbitals, respectively. Similar to previous reports [28,29], the peaks at 710.7 and 723.9 eV are corresponding to $\text{Fe } 2p_{3/2}$ and $\text{Fe } 2p_{1/2}$ orbitals of Fe^{2+} ions. The high content of Fe^{2+} is thought to couple with the neighboring N atoms to form the Fe-N_x active center with superior ORR activity [29–31]. The binding energies of Fe^{3+} species are found to be at around 713.2 and 726.8 eV for the $2p_{3/2}$ and $2p_{1/2}$ orbitals, respectively, which come from the inevitable oxidation of the zero-valence iron or Fe^{2+} ions by air. There are two kinds of nitrogen-doping species, including N-doped carbon and N-coordinated Fe

species. As shown in Fig. 2e, compared with the precursor $\text{Zn}_3[\text{Fe}(\text{CN})_6]_2$, the major N 1s peak in the $\text{Fe}/\text{Fe}_5\text{C}_2@\text{N-C}$ shifts a little to higher binding energy, indicating a transformation of CN complex within Prussian blue analogue to nitrogen heteroatom embedded into carbon, thus accompanying with new bond formation of Fe-N_x and N–C active sites [12]. The high-resolution N 1s spectrum can be divided into five peaks at 398.6, 399.1, 399.9, 401.2 and 404.4 eV, which are ascribed to pyridinic-N, Fe-N_x , pyrrolic-N, graphitic-N and oxidized N species, respectively [28,29,32–34]. As shown in Fig. 2e, higher temperature would cause relatively higher content of graphitic-N but relatively lower content of pyridinic-N and Fe-N_x . The high-resolution C 1s spectrum of $\text{Fe}/\text{Fe}_5\text{C}_2@\text{N-C}$ in Fig. S4 are centered at around 284.6 eV with an asymmetric tail at about 290 eV, demonstrating the existence of N and O heteroatoms in the carbon matrix. After deconvolution, they can be fitted into four peaks at 284.72, 285.02, 286.1 and 290.2 eV, corresponding to C–C&C=C, C–N&C–O, C=O&C=N and O=C–O, respectively [35,36]. The relatively narrow C–C peaks and reduced C–O/C=O species in high annealing temperatures indicate the increasing of the degree of carbon graphitization. The BET specific surface area of $\text{Fe}/\text{Fe}_5\text{C}_2@\text{N-C-1000}$ is calculated to be $712.4 \text{ m}^2 \text{ g}^{-1}$ on the base of nitrogen adsorption/desorption isotherms (Fig. 2f), which is higher than values of as-prepared $\text{Fe}/\text{Fe}_5\text{C}_2@\text{N-C-1000}$ without the process of acid washing and second heat-treatment (Fig. S5 and Table S3). The BJH pore size distribution curve derived from the N_2 absorption confirms the presence of both micro-pores and mesopores as shown in the inset of Fig. 2f.

As shown Fig. 3, we systematically studied the morphology features and inner structure of our catalyst. Fig. 3a and b display the SEM and TEM images of the precursor $\text{Zn}_3[\text{Fe}(\text{CN})_6]_2$ synthesized with a liquid phase precipitation method. The obtained $\text{Zn}_3[\text{Fe}(\text{CN})_6]_2$ is found to exist in the form of uniform particles with a spherical morphology, whose particle size is about 250 nm. As shown in Fig. 3c and d, the $\text{Fe}/\text{Fe}_5\text{C}_2@\text{N-C-1000}$ is observed to become porous caused by zinc metal volatilization and to consist of inner particles and outside graphitic carbon layers like rings or tubes. The SEM images are displayed in Fig. S6, demonstrating that $\text{Fe}/\text{Fe}_5\text{C}_2@\text{N-C-900}$ can retain to a great extent the spherical morphology of the precursor while $\text{Fe}/\text{Fe}_5\text{C}_2@\text{N-C-1000}$ exhibits a rough and porous morphology. As shown in the higher-resolution TEM images of Fig. 3e and f, the dark particle is wrapped by the graphitic rings and the particle is crystallized with an inter-layer spacing of 0.202 nm, which is ascribed to (110) facet of iron (PDF#06-0696), which is in accordance with the result of XRD. In this architecture, the thin carbon shells can avoid the direct exposure of iron sites to the electrolyte and preserve the structural and inter-facial stabilization of iron nanoparticles. The elements distribution on the carbon

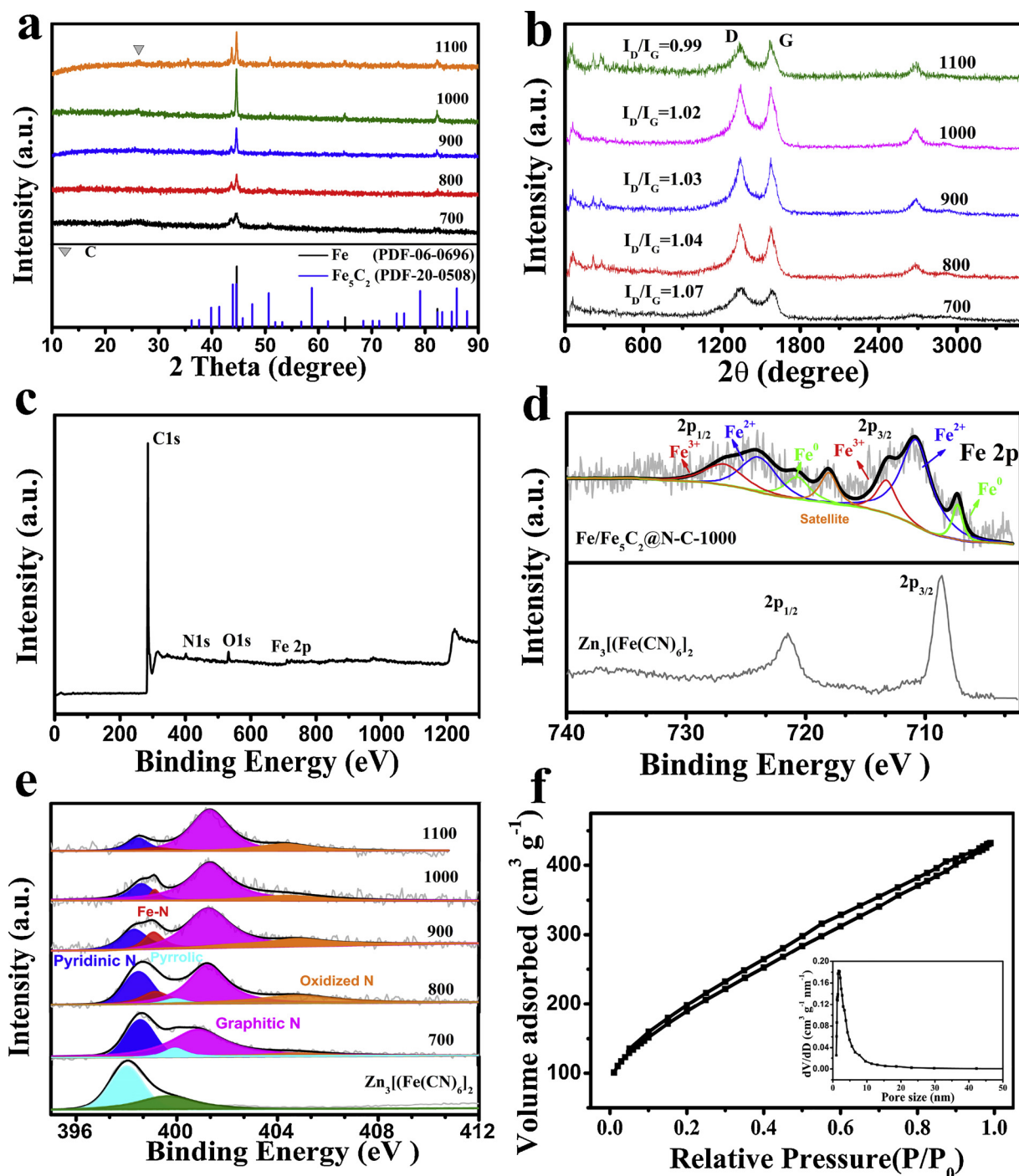


Fig. 2. (a) XRD patterns, (b) Raman spectra, (c) XPS survey spectrum and (d) the high resolution N 1s spectra of Fe/Fe₅C₂@N-C catalysts prepared at various temperatures (700–1100 °C). (e) the high resolution Fe 2p XPS spectra of Fe/Fe₅C₂@N-C-1000 and the precursor Zn₃[(Fe(CN)₆)]₂. (f) the nitrogen adsorption-desorption isotherm of Fe/Fe₅C₂@N-C-1000. Its inset shows the corresponding pore size distribution curve.

matrix is revealed by EDX elemental mapping analysis. As shown in Fig. 3g, nitrogen is uniformly dispersed over the whole carbon matrix while iron is mainly distributed in the form of small particles.

In order to study the electrocatalytic performance of Fe/Fe₅C₂@N-C, linear sweep voltammetry (LSV) measurements were carried out by RDE/RRDE techniques from 1.2 to 0 V with a predefined rotation rate at a scan rate of 10 mV s⁻¹. As shown in Fig. 4a, Fe/Fe₅C₂@N-C-1000 has the highest ORR activity, which is even better than Pt/C. As shown in Fig. 4b, Fe/Fe₅C₂@N-C-1000 shows a low Tafel slope of 57 mV dec⁻¹, which is just a little higher than that of Pt/C. As displayed in Fig. 4c, Fe/Fe₅C₂@N-C-800 and Fe/Fe₅C₂@N-C-900 have larger limited current

densities (J_d), while Fe/Fe₅C₂@N-C-1000 exhibits the best ORR activity with an half-wave potential (E_{1/2}) of 0.85 V, which is more positive than that of Pt/C (0.83 V). We tested the RDE polarization curves at a series of rotation speeds from 400 to 2025 rpm to explore the kinetic parameters during ORR (Fig. S6) and to obtain the Koutecky–Levich (K–L) plots (Fig. 4d). According to the K–L equations (described in the supporting information), the estimated transferred electrons numbers per molecule O₂ are 3.58, 3.59, 3.62 and 3.65 at 0.3 V, 0.4 V, 0.5 V and 0.6 V, respectively, which are slightly lower than Pt/C (4.0 at 0.3 V). The RRDE measurement was conducted to determine the transferred electron number and H₂O₂ yield. Fig. 4e displays the RRDE

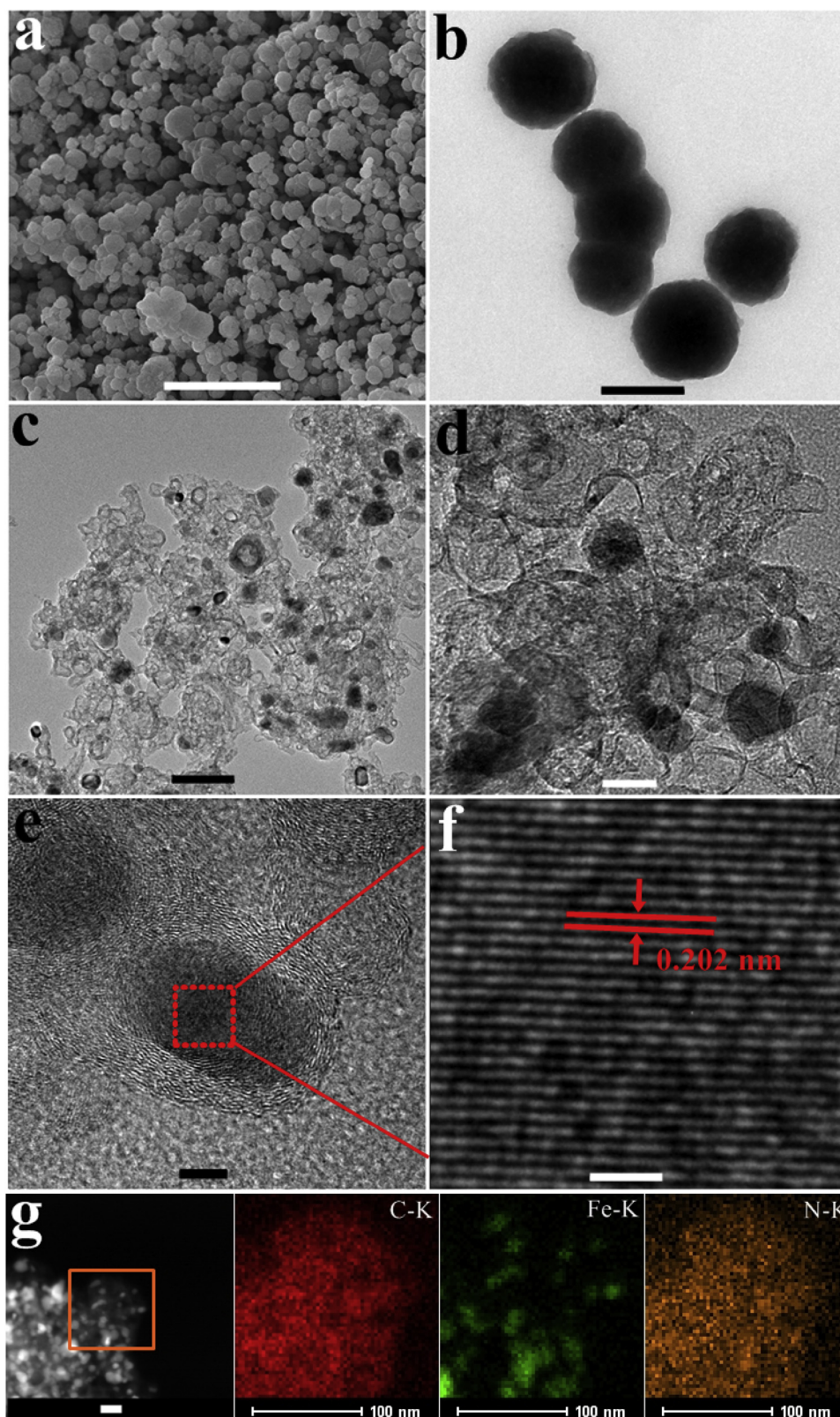


Fig. 3. (a) SEM and (b) TEM image of the precursor $\text{Zn}_3[\text{Fe}(\text{CN})_6]_2$. (c–f) Low and high resolution TEM image of $\text{Fe}/\text{Fe}_5\text{C}_2@\text{N-C-1000}$. (g) Elemental mapping images of $\text{Fe}/\text{Fe}_5\text{C}_2@\text{N-C-1000}$. Scale bars: 2 μm (a), 200 nm (b), 100 nm (c), 20 nm (d), 5 nm (e), 1 nm (f) and 50 nm (g).

voltammograms of $\text{Fe}/\text{Fe}_5\text{C}_2@\text{N-C-1000}$ and commercial 20% Pt/C, from which the corresponding H_2O_2 yield and transferred electron number are calculated (Fig. 4f). The transferred electron number over $\text{Fe}/\text{Fe}_5\text{C}_2@\text{N-C-1000}$ is above 3.84 and H_2O_2 yield is below 8.1% at the

whole potential range, which are close to that of Pt/C. Apart from the ORR activity in the alkaline media, we also tested the ORR performance in 0.1 M HClO_4 . As can be seen in Fig. S8, $\text{Fe}/\text{Fe}_5\text{C}_2@\text{N-C-800}$ is found to have the highest activity with the $E_{1/2}$ of 0.66 V, thus different from

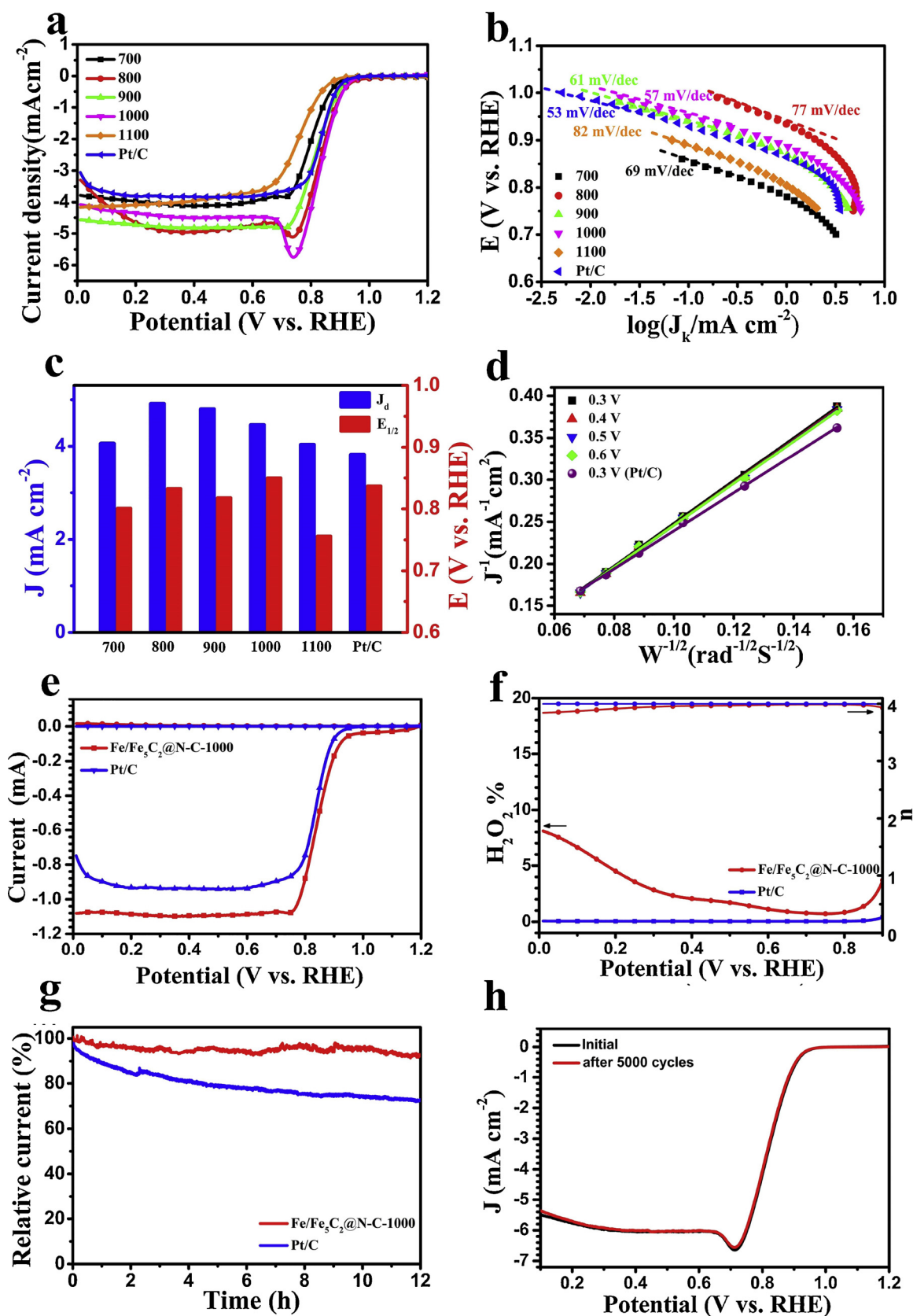


Fig. 4. (a) RDE LSV curves for Fe/Fe₅C₂@N-C-700, Fe/Fe₅C₂@N-C-800, Fe/Fe₅C₂@N-C-900, Fe/Fe₅C₂@N-C-1000, Fe/Fe₅C₂@N-C-1100 and commercial 20% Pt/C catalysts at a rotating speed of 900 rpm. (b) Tafel slopes of the different Fe/Fe₅C₂@N-C samples and Pt/C catalyst and (c) the diffusion limiting current (J_d), half-wave potential (E_{1/2}) of all the samples derived from (a). (d) the K-L plots at various potentials for Fe/Fe₅C₂@N-C-1000 and commercial 20% Pt/C catalyst. (e) RRDE voltammograms of the ORR on Fe/Fe₅C₂@N-C-1000 and commercial 20% Pt/C at 900 rpm. (f) Peroxide yields and transferred electron numbers of Fe/Fe₅C₂@N-C-1000 and commercial 20% Pt/C. (g) I-t plots (normalized to the initial current) of Fe/Fe₅C₂@N-C-1000 and Pt/C at 0.6 V, performed at the rotation speed of 1600 rpm. (h) ORR polarization curves of Fe/Fe₅C₂@N-C-1000 at the rotation speed of 1600 rpm before and after 5000 CV cycles. All the measurements were conducted in 0.1 M KOH solution.

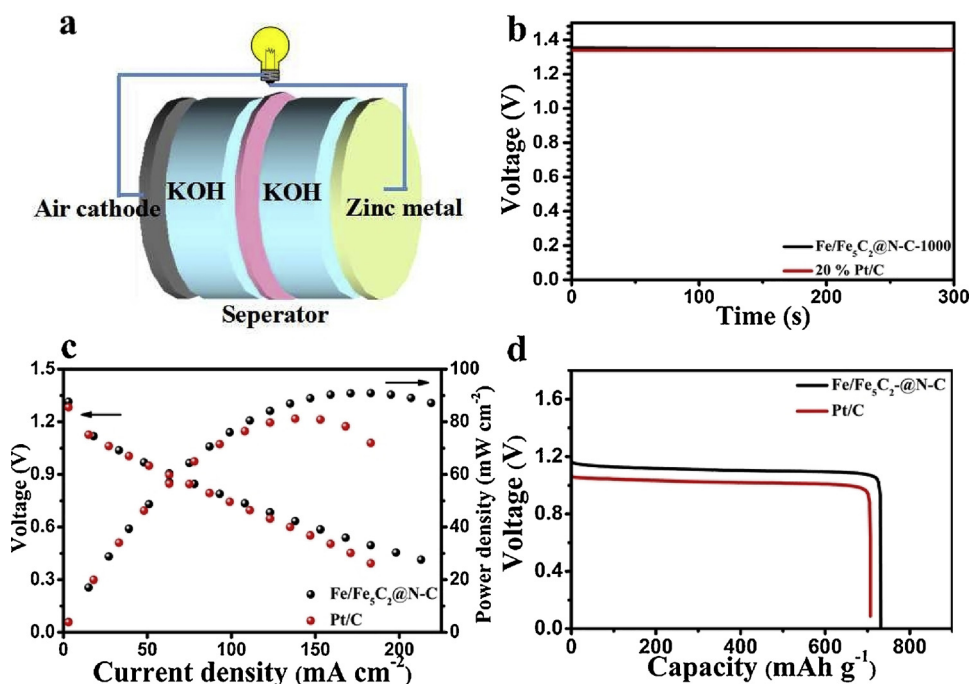


Fig. 5. (a) Schematic configuration of the zinc-air battery. (b) Open potential-time curves, (c) Polarization/power density curves, (d) Discharge curves of the zinc-air batteries using Pt/C and Fe/Fe₅C₂@N-C-1100 as ORR catalysts.

the result in alkaline media. According to previously reported works, both N-doped carbon (including pyridinic N and graphitic N) and MeN_xC_y moieties are thought to be the active sites in alkaline media [37–40]. However, only MeN_xC_y moieties are proved to have good performance in acidic media [41]. Therefore, the relatively poorer activity is usually obtained in acidic media [42–44]. As displayed in Table S1, we calculated the contents of different active N dopants on the base of N1 s XPS spectrum. The highest content of FeN_xC_y moieties, related to acidic ORR activity, is obtained at 800 °C, which may explain why the best pyrolytic temperature for ORR in acidic media is 800 °C. Compared with the ORR process in acidic solution, the ORR active sites in the alkaline media are usually much more abundant. So, the activity in alkaline media is determined not only by the active sites contents but also by the other factors such as graphitization degree, porous structure and the facilitating effect from the inside Fe/Fe₅C₂ nanoparticles. The effect of catalytic graphitization on amorphous carbon by iron species can be shown from the XRD pattern and HRTEM images, which has been widely reported to improve electrochemical performance [44,45]. The enhancing effect of the inside Fe/Fe₅C₂ nanoparticles to facilitate ORR activity has been also reported in previous works, which is thought to be a synergistic effect between the outside N-doped carbon and inside nanoparticles [42,46]. Zinc is thought to construct a porous structure in the matrix to improve the dispersity of the active species. In order to make clear the effect of zinc on the activity, we prepared the control sample Fe₃[Fe(CN)₆]₂-1000 by annealing Fe₃[Fe(CN)₆]₂ at 1000 °C. As shown in Fig. S9a and Table S2, Fe₃[Fe(CN)₆]₂-1000 has the similar phase composition and BET surface area with Fe/Fe₅C₂@N-C-1000. The TEM images in Fig. S9b and c demonstrate that the decomposition of Fe₃[Fe(CN)₆]₂ would lead to the formation of a mass of carbon nanotubes but leave severely agglomerated iron species particles, which may be due to the superfluous Fe sites in the Fe₃[Fe(CN)₆]₂ precursor. The lack of dilution effect from zinc results in larger iron species particles in Fe₃[Fe(CN)₆]₂-1000 than Fe/Fe₅C₂@N-C-1000. The ORR catalytic performances of Fe/Fe₅C₂@N-C-1000 and Fe₃[Fe(CN)₆]₂-1000 were compared in Fig. S9d, indicating a much higher activity of Fe/Fe₅C₂@N-C-1000. In addition, we can also find the rougher and more porous surface of Fe/Fe₅C₂@N-C-1000 than Fe/Fe₅C₂@N-C-900 as shown in Fig. S6, which is because zinc just volatilize at 1000 °C. This

is why Fe/Fe₅C₂@N-C-1000 is more active than Fe/Fe₅C₂@N-C-900. Therefore, the good dispersity of the active species and porous structure are caused by the volatile zinc, thus exposing more active sites and providing favourable access to reactants and electrolyte. The best activity of Fe/Fe₅C₂@N-C-1000 in alkaline media is ascribed to the synergism of optimum N-doping level, favorable porous structure, high dispersity of active sites and the facilitating effect from the inside Fe/Fe₅C₂ nanoparticles. The comparison of Fe/Fe₅C₂@N-C-1000 and the state of the art catalysts reported in the literature is provided in Table S3.

Durability is usually evaluated by the I-t chronoamperometric response, according to the previous reports [47,48]. As shown in Fig. 4g, Fe/Fe₅C₂@N-C-1000 and Pt/C keep 91.9% and 72.8% retention of the initial ORR currents after 12 h, respectively. The continuous operation on low potential might have caused migration/aggregation of the Pt nanoparticles and subsequent loss of the specific catalytic activity for Pt/C catalyst. However, Fe/Fe₅C₂@N-C-1000 demonstrates superior stability due to the favorable metal@carbon structure. In addition, the Fe/Fe₅C₂@N-C-1000 electrode shows almost identical polarization curves before and after the 5000 continuous potential cycles in O₂-saturated solution (Fig. 4h). The resistance to methanol crossover effect was evaluated by a chronoamperometric curve (normalized to the initial current) performed at 1600 rpm by injecting of 3 M methanol into the electrolyte. As shown in Fig. S10, Fe/Fe₅C₂@N-C-1000 exhibits much better resistibility to methanol. The above results indicate Fe/Fe₅C₂@N-C-1000 having an excellent activity, a high durability and an outstanding methanol resistance. We ascribe the high durability to the special structure, wherein the Fe/Fe₅C₂ is protected by the thin N-doped graphitic layer, thus keeping a stable electrochemical condition.

We applied Fe/Fe₅C₂@N-C-1000 as the air-electrode materials in a coin-cell zinc-air battery, which is schematically shown in Fig. 5a. The open circuit potential-time curves of the zinc-air batteries using Fe/Fe₅C₂@N-C-1000 and Pt/C as the catalysts are exhibited in Fig. 5b, indicating the similar values of the open circuit potentials. The polarization and the corresponding power density profiles in Fig. 5c show the zinc-air battery using the Fe/Fe₅C₂@N-C-1000 catalyst with a peak-power density of 91 mW cm⁻², slightly higher than that of Pt/C catalyst (81.3 mW cm⁻²). The discharge curves in Fig. 5d demonstrate that the

zinc-air battery with the Fe/Fe₅C₂@N-C-1000 catalyst exhibits a voltage plateau of ~ 1.1 V at a current density of 10 mA cm⁻². In addition, the specific capacity of the zinc-air battery with Fe/Fe₅C₂@N-C-1000 catalyst is determined to be 732 mA h g Zn⁻¹, close to the theoretical discharge capacity (820 mA h g Zn⁻¹) [17].

4. Conclusions

In summary, Fe/Fe₅C₂ wrapped in N-doped carbon (Fe/Fe₅C₂@N-C) was fabricated by annealing decomposition of a zinciferous Prussian blue analogue Zn₃[Fe(CN)₆]₂. The obtained Fe/Fe₅C₂@N-C-1000 catalyst exhibits an excellent ORR activity and a superior stability, especially in alkaline electrolyte, which are due to the rich iron/iron carbide particles and protective N-doped graphitic carbon shells. In addition, served as an air cathode material for zinc-air battery, Fe/Fe₅C₂@N-C-1000 demonstrates a remarkable discharge performance. Due to the structural merits and efficient electrocatalytic properties, this strategy holds great promise for the development of non-precious metal electrocatalysts of fuel cells and metal-air batteries.

Acknowledgements

This work was financially supported by the National Natural Science Foundation of China (11575084 and 51602153), the Natural Science Foundation of Jiangsu Province (BK20160795), Nanjing University of Aeronautics and Astronautics PhD Short-term Visiting Scholar Project, Funding of Jiangsu Innovation Program for Graduate Education (KYCX17.0250), Funding for Outstanding Doctoral Dissertation in NUAA (BCXJ17-09) and A Project Funded by the Priority Academic Program Development of Jiangsu Higher Education Institutions (PAPD).

Appendix A. Supplementary data

Supplementary material related to this article can be found, in the online version, at doi:<https://doi.org/10.1016/j.apcatb.2018.11.005>.

References

- [1] M. Escudero-Escribano, P. Malacrida, M.H. Hansen, U.G. Vej-Hansen, A. Velázquez-Palenzuela, V. Tripkovic, J. Schiotz, J. Rossmeisl, I.E. Stephens, I. Chorkendorff, Tuning the activity of Pt alloy electrocatalysts by means of the lanthanide contraction, *Science* 352 (2016) 73–76.
- [2] X. Huang, Z. Zhao, L. Cao, Y. Chen, E. Zhu, Z. Lin, M. Li, A. Yan, A. Zettl, Y.M. Wang, High-performance transition metal-doped Pt₃Ni octahedra for oxygen reduction reaction, *Science* 348 (2015) 1230–1234.
- [3] X.X. Wang, S. Hwang, Y.-T. Pan, K. Chen, Y. He, S.G. Karakalos, H. Zhang, J.S. Spendlow, D. Su, G. Wu, Ordered Pt₃Co intermetallic nanoparticles derived from metal-organic frameworks for oxygen reduction, *Nano Lett.* 18 (2018) 4163–4171.
- [4] J. Zhang, Z. Zhao, Z. Xia, L. Dai, A metal-free bifunctional electrocatalyst for oxygen reduction and oxygen evolution reactions, *Nat. Nanotechnol.* 10 (2015) 444–452.
- [5] K. Gong, F. Du, Z. Xia, M. Durstock, L. Dai, Nitrogen-doped carbon nanotube arrays with high electrocatalytic activity for oxygen reduction, *Science* 323 (2009) 760–764.
- [6] S. Roy, A. Bandyopadhyay, M. Das, P.P. Ray, S.K. Pati, T.K. Maji, Redox-active and semi-conducting donor-acceptor conjugated microporous polymers as metal-free ORR catalysts, *J. Mater. Chem. A* 6 (2018) 5587–5591.
- [7] G. Wu, K.L. More, C.M. Johnston, P. Zelenay, High-performance electrocatalysts for oxygen reduction derived from polyaniline, iron, and cobalt, *Science* 332 (2011) 443–447.
- [8] Y. Han, Y.-G. Wang, W. Chen, R. Xu, L. Zheng, J. Zhang, J. Luo, R.-A. Shen, Y. Zhu, W.-C. Cheong, Hollow N-doped carbon spheres with isolated cobalt single atomic sites: superior electrocatalysts for oxygen reduction, *J. Am. Chem. Soc.* 139 (2017) 17269–17272.
- [9] Y. Chen, S. Ji, C. Chen, Q. Peng, D. Wang, Y. Li, Single-atom catalysts: synthetic strategies and electrochemical applications, *Joule* 2 (2018) 1242–1264.
- [10] Y. Han, Y. Wang, R. Xu, W. Chen, L. Zheng, A. Han, Y. Zhu, J. Zhang, H. Zhang, J. Luo, Electronic structure engineering to boost oxygen reduction activity by controlling the coordination of the central metal, *Energy Environ. Sci.* 11 (2018) 2348–2352.
- [11] A. Han, W. Chen, S. Zhang, M. Zhang, Y. Han, J. Zhang, S. Ji, L. Zheng, Y. Wang, L. Gu, A polymer encapsulation strategy to synthesize porous nitrogen-doped carbon-nanosphere-supported metal isolated-single-atomic-site catalysts, *Adv. Mater.* 30 (2018) 1706508.
- [12] H. Zhang, S. Hwang, M. Wang, Z. Feng, S. Karakalos, L. Luo, Z. Qiao, X. Xie, C. Wang, D. Su, Single atomic iron catalysts for oxygen reduction in acidic media: particle size control and thermal activation, *J. Am. Chem. Soc.* 139 (2017) 14143–14149.
- [13] Y. Chen, S. Ji, Y. Wang, J. Dong, W. Chen, Z. Li, R. Shen, L. Zheng, Z. Zhuang, D. Wang, Isolated single iron atoms anchored on N-doped porous carbon as an efficient electrocatalyst for the oxygen reduction reaction, *Angew. Chem. Int. Ed.* 56 (2017) 6937–6941.
- [14] S. Li, C. Cheng, X. Zhao, J. Schmidt, A. Thomas, Active salt/silica-templated 2D mesoporous FeCo-N_x-carbon as bifunctional oxygen electrodes for zinc-air batteries, *Angew. Chem. Int. Ed.* 57 (2018) 1856–1862.
- [15] X. Fan, Z. Peng, R. Ye, H. Zhou, X. Guo, M₃C (M: Fe, Co, Ni) nanocrystals encased in graphene nanoribbons: an active and stable bifunctional electrocatalyst for oxygen reduction and hydrogen evolution reactions, *ACS Nano* 9 (2015) 7407–7418.
- [16] W.-J. Jiang, L. Gu, L. Li, Y. Zhang, X. Zhang, L.-J. Zhang, J.-Q. Wang, J.-S. Hu, Z. Wei, L.-J. Wan, Understanding the high activity of Fe–N–C electrocatalysts in oxygen reduction: Fe/Fe₃C nanoparticles boost the activity of Fe–N_x, *J. Am. Chem. Soc.* 138 (2016) 3570–3578.
- [17] M. Zhang, Q. Dai, H. Zheng, M. Chen, L. Dai, Novel MOF-derived Co@N-C bifunctional catalysts for highly efficient Zn–Air batteries and water splitting, *Adv. Mater.* 30 (2018) 1705431.
- [18] Y. Niu, X. Huang, W. Hu, Fe₃C nanoparticle decorated Fe/N doped graphene for efficient oxygen reduction reaction electrocatalysis, *J. Power Sources* 332 (2016) 305–311.
- [19] H. Wang, W. Wang, Y.Y. Xu, S. Dong, J. Xiao, F. Wang, H. Liu, B.Y. Xia, Hollow nitrogen-doped carbon spheres with Fe₃O₄ nanoparticles encapsulated as a highly active oxygen-reduction catalyst, *ACS Appl. Mater. Interfaces* 9 (2017) 10610–10617.
- [20] Q. Guo, F. Liang, X.-Y. Gao, Q.-C. Gan, X.-B. Li, J. Li, Z. Lin, C.-H. Tung, L.-Z. Wu, Metallic Co₂C: a promising cocatalyst to boost photocatalytic hydrogen evolution of colloidal quantum dots, *ACS Catal.* 8 (2018) 5890–5895.
- [21] W. Ahn, M.G. Park, D.U. Lee, M.H. Seo, G. Jiang, Z.P. Cano, F.M. Hassan, Z. Chen, Hollow Multivoid nanocuboids derived from ternary Ni–Co–Fe Prussian blue analog for dual-electrocatalysis of oxygen and hydrogen evolution reactions, *Adv. Funct. Mater.* 28 (2018) 1802129.
- [22] Y. Ge, P. Dong, S.R. Craig, P.M. Ajayan, M. Ye, J. Shen, Transforming nickel hydroxide into 3D Prussian blue analogue array to obtain Ni₂P/Fe₂P for efficient hydrogen evolution reaction, *Adv. Energy Mater.* 8 (2018) 1800484.
- [23] D. Su, M. Cortie, G. Wang, Fabrication of N-doped graphene–carbon nanotube hybrids from Prussian blue for lithium–sulfur batteries, *Adv. Energy Mater.* 7 (2017) 1602014.
- [24] C. Ng, J. Ding, Y. Shi, L. Gan, Structure and magnetic properties of copper (III) hexacyanoferrate (III) compound, *J. Phys. Chem. Solids* 62 (2001) 767–775.
- [25] P. Xiong, G. Zeng, L. Zeng, M. Wei, Prussian blue analogues Mn[Fe(CN)₆]_{0.6667}nH₂O cubes as an anode material for lithium-ion batteries, *Dalton Trans.* 44 (2015) 16746–16751.
- [26] C. Ng, J. Ding, L. Gan, Structure and magnetic properties of Zn–Fe cyanide, *J. Phys. D: Appl. Phys.* 34 (2001) 1188–1192.
- [27] J. Tang, R.R. Salunkhe, J. Liu, N.L. Torad, M. Imura, S. Furukawa, Y. Yamauchi, Thermal conversion of core-shell metal–organic frameworks: a new method for selectively functionalized nanoporous hybrid carbon, *J. Am. Chem. Soc.* 137 (2015) 1572–1580.
- [28] L. Lin, Q. Zhu, A.-W. Xu, Noble-metal-free Fe–N/C catalyst for highly efficient oxygen reduction reaction under both alkaline and acidic conditions, *J. Am. Chem. Soc.* 136 (2014) 11027–11033.
- [29] S. Han, X. Hu, J. Wang, X. Fang, Y. Zhu, Novel route to Fe-based cathode as an efficient bifunctional catalysts for rechargeable Zn–air battery, *Adv. Energy Mater.* (2018) 1800955.
- [30] U.I. Koslowski, I. Abs-Wurmbach, S. Fiechter, P. Bogdanoff, Nature of the catalytic centers of porphyrin-based electrocatalysts for the ORR: a correlation of kinetic current density with the site density of Fe–N_x centers, *J. Phys. Chem. C* 112 (2008) 15356–15366.
- [31] J. Xu, C. Wu, Q. Yu, Y. Zhao, X. Li, L. Guan, Ammonia defective etching and nitrogen-doping of porous carbon toward high exposure of heme-derived Fe–N_x site for efficient oxygen reduction, *ACS Sustain. Chem. Eng.* 6 (2017) 551–560.
- [32] C. Zhang, J. Liu, Y. Ye, Z. Aslam, R. Brydson, C. Liang, Fe–N-doped mesoporous carbon with dual active sites loaded on reduced graphene oxides for efficient oxygen reduction catalysts, *ACS Appl. Mater. Interfaces* 10 (2018) 2423–2429.
- [33] H. Ren, Y. Wang, Y. Yang, X. Tang, Y. Peng, H. Peng, L. Xiao, J. Lu, H.D. Abruna, L. Zhuang, Fe/N/C nanotubes with atomic Fe sites: a highly active cathode catalyst for alkaline polymer electrolyte fuel cells, *ACS Catal.* 7 (2017) 6485–6492.
- [34] W. Liu, L. Zhang, X. Liu, X. Liu, X. Yang, S. Miao, W. Wang, A. Wang, T. Zhang, Discriminating catalytically active FeN_x species of atomically dispersed Fe–N–C catalyst for selective oxidation of the C–H bond, *J. Am. Chem. Soc.* 139 (2017) 10790–10798.
- [35] J. Chen, J. Xu, S. Zhou, N. Zhao, C.-P. Wong, Nitrogen-doped hierarchically porous carbon foam: a free-standing electrode and mechanical support for high-performance supercapacitors, *Nano Energy* 25 (2016) 193–202.
- [36] Z. Lin, G. Waller, Y. Liu, M. Liu, C.P. Wong, Facile synthesis of nitrogen-doped graphene via pyrolysis of graphene oxide and urea, and its electrocatalytic activity toward the oxygen-reduction reaction, *Adv. Energy Mater.* 2 (2012) 884–888.
- [37] L. Lai, J.R. Potts, D. Zhan, L. Wang, C.K. Poh, C. Tang, H. Gong, Z. Shen, J. Lin, R.S. Ruoff, Exploration of the active center structure of nitrogen-doped graphene-based catalysts for oxygen reduction reaction, *Energy Environ. Sci.* 5 (2012) 7936–7942.

- [38] T. Xing, Y. Zheng, L.H. Li, B.C. Cowie, D. Gunzelmann, S.Z. Qiao, S. Huang, Y. Chen, Observation of active sites for oxygen reduction reaction on nitrogen-doped multilayer graphene, *ACS Nano* 8 (2014) 6856–6862.
- [39] H.B. Yang, J. Miao, S.-F. Hung, J. Chen, H.B. Tao, X. Wang, L. Zhang, R. Chen, J. Gao, H.M. Chen, L.M. Dai, B. Liu, Identification of catalytic sites for oxygen reduction and oxygen evolution in N-doped graphene materials: development of highly efficient metal-free bifunctional electrocatalyst, *Sci. Adv.* 2 (2016) e1501122.
- [40] T.S. Olson, S. Pylypenko, P. Atanasov, K. Asazawa, K. Yamada, H. Tanaka, Anion-exchange membrane fuel cells: dual-site mechanism of oxygen reduction reaction in alkaline media on cobalt–polypyrrole electrocatalysts, *J. Phys. Chem. C* 114 (2010) 5049–5059.
- [41] A. Zitolo, V. Goellner, V. Armel, M.-T. Sougrati, T. Mineva, L. Stievano, E. Fonda, F. Jaouen, Identification of catalytic sites for oxygen reduction in iron-and nitrogen-doped graphene materials, *Nat. Mater.* 14 (2015) 937.
- [42] Y. Hu, J.O. Jensen, W. Zhang, L.N. Cleemann, W. Xing, N.J. Bjerrum, Q. Li, Hollow spheres of iron carbide nanoparticles encased in graphitic layers as oxygen reduction catalysts, *Angew. Chem. Int. Ed.* 53 (2014) 3675–3679.
- [43] M. Xiao, J. Zhu, L. Feng, C. Liu, W. Xing, Meso/macroporous nitrogen–doped carbon architectures with iron carbide encapsulated in graphitic layers as an efficient and robust catalyst for the oxygen reduction reaction in both acidic and alkaline solutions, *Adv. Mater.* 27 (2015) 2521–2527.
- [44] G. Ren, X. Lu, Y. Li, Y. Zhu, L. Dai, L. Jiang, Porous core–shell Fe₃C embedded N-doped carbon nanofibers as an effective electrocatalysts for oxygen reduction reaction, *ACS Appl. Mater. Interfaces* 8 (2016) 4118–4125.
- [45] J. Yuan, C. Giordano, M. Antonietti, Ionic liquid monomers and polymers as precursors of highly conductive, mesoporous, graphitic carbon nanostructures, *Chem. Mater.* 22 (2010) 5003–5012.
- [46] E. Hu, X.Y. Yu, F. Chen, Y. Wu, Y. Hu, X.W. Lou, Graphene layers–wrapped Fe/Fe₅C₂ nanoparticles supported on n–doped graphene nanosheets for highly efficient oxygen reduction, *Adv. Energy Mater.* 8 (2018) 1702476.
- [47] B. Li, S. Chen, J. Tian, M. Gong, H. Xu, L. Song, Amorphous nickel-iron oxides/carbon nanohybrids for an efficient and durable oxygen evolution reaction, *Nano Res.* 10 (2017) 3629–3637.
- [48] D. Liu, C. Wu, S. Chen, S. Ding, Y. Xie, C. Wang, T. Wang, Y.A. Haleem, Z. ur Rehman, Y. Sang, In situ trapped high-density single metal atoms within graphene: iron-containing hybrids as representatives for efficient oxygen reduction, *Nano Res.* 11 (2018) 2217–2228.